WoldeGabriel et al. 1996
ER ID# 54427
(27)

Submitted to the N.M. Geological Society 1996 Volume Giday



Excerpt. LA-UR-96

# TEMPORAL AND GEOCHEMICAL TRENDS OF LAVAS IN WHITE ROCK CANYON AND THE PAJARITO PLATEAU, JEMEZ VOLCANIC FIELD, NEW MEXICO, USA

GIDAY WOLDEGABRIEL[1], A. WILLIAM LAUGHLIN[2], DAVID P. DETHIER[3], AND MATTHEW HEIZLER[4]

[1] EES-1/D462, Los Alamos National Laboratory, Los Alamos, NM 87545

[2] ICF Kaiser Engineers Inc., Los Alamos, NM 87544

[3] Williams College, Williamstown, MA 01267

[4] New Mexico Bureau New Bureau of Mines, New Mexico Institute of Mining and Technology, Socorro, NM 87801

## ABSTRACT

$^{40}Ar/^{39}Ar$ dates and geochemical analyses provide insights into the geochronology and petrologic evolution of Miocene-Pliocene volcanism in the vicinity of White Rock Canyon and the adjacent Pajarito Plateau. Lava flows and some dikes were sampled from several stratigraphic sections in this study area. $^{40}Ar/^{39}Ar$ results indicate 3 distinct pulses of volcanic activities at 9.3, 2.8 and 2.6-2.3 Ma. A single 9.3 Ma mugearitic lava flow occurs only locally, whereas the Pliocene volcanism is voluminous, widespread, and geochemically diverse. The earlier (2.8-2.4 Ma) Pliocene lavas are predominantly evolved compositions (hawaiite, mugearite, benmorite, and dacite), whereas the lastest (2.5-2.3 Ma) and stratigraphically uppermost flows are entirely tholeiitic basalts.

The 9.3 Ma mugearite lava was erupted coevally with intense late Miocene (10-7 Ma) magmatic and tectonic activities in the Jemez volcanic field. The Pliocene (2.8-2.3 Ma) rift-bound volcanism appears to be contemporaneous with initiation of movement along the Pajarito fault zone. Despite the temporal similarities and geographic proximity, the geochemical diversity of the White Rock Canyon volcanic rocks reflects different magmatic sources modified by differentiation and crustal contamination.

7374

Received by ER-RPF
JUN 10 1996

## INTRODUCTION

The Jemez volcanic field contains mafic, intermediate, and silicic rocks of the Keres (>13 to 6 Ma), Polvadera (14-2 Ma), and Tewa (1.6 to 0.13 Ma) Groups (Gardner et al., 1986; Goff et al., 1989; Aldrich and Dethier, 1990; Izett and Obradovich, 1994). The eastern part of this volcanic field is represented by the Pajarito Plateau. The plateau consists of Miocene sedimentary rocks of the Santa Fe Group and the Pliocene volcanic fanglomerates and conglomerates of the Puye Formation which are interbedded with Cerros del Rio and Pajarito Plateau volcanic rock deposits (Dethier, 1996; Reneau et al., 1995). These older units are blanketed by the Plio-Pleistocene Bandelier and post-Bandelier Tuff pyroclastic rocks and Quaternary alluvial fan, colluvial, and landslide deposits. All of these units are exposed in 200 to 300-m-deep and steep-sided canyons that merge with the White Rock Canyon of the Rio Grande along the eastern part of the Pajarito Plateau. Late Pliocene K-Ar ages (2.0-2.8 Ma) were reported on samples from these volcanic rocks (Manley, 1976; Bachman and Mehnert, 1978; Dethier, 1996). In addition, an age of 4.4 Ma was reported from a deeply-eroded vent and maar (Black Mesa at San Ildefonso) at the northern part of the Cerros del Rio volcanic field about 5 km upstream from the Otowi Bridge (Baldridge et al., 1980).

Chemical and petrologic data from the major units of the Jemez volcanic field exhibit a range of hy-and ne-normative compositions intermediate between subalkali tholeiites and alkali olivine basalts (Baldridge et al., 1995). Compositionally variable volcanic rocks are present in the Cerros del Rio volcanic field and this diversity was interpreted to indicate eruptions from different magmatic source areas (Aubele, 1979; Duncker et al., 1991; Baldridge et al., 1995).

The Pajarito Plateau is separated from the Jemez volcanic field by the Pajarito fault zone (Fig. 1). This fault system trends north-northeast with down-to-the east displacement that was initiated in the late Miocene time (5 Ma) and cuts Neogene and Quaternary volcanic and sedimentary rocks along the western rift shoulder of the Española Basin (Manley, 1979; Golombeck, 1983; Gardner and Goff, 1984; Aldrich and Dethier, 1990). Moreover, a now-buried NNE-trending marginal graben was delineated by gravity measurements under the Pajarito Plateau

(Budding, 1978). Recent gravity data suggest three narrow and deep structural sub-basins along the Pajarito and Embudo fault zones (Ferguson et al., 1995). **(insert Fig. 1 here)**

For this study, lava flows from White Rock Canyon, the Cerros del Rio volcanic field, and the Pajarito Plateau (Fig. 1) were collected , dated by the $^{40}Ar/^{39}Ar$ method, and geochemically analyzed. This effort is part of the Los Alamos National Laboratory Environmental Restoration Project and attempts to determine the volcanic and tectonic histories of the Pajarito Plateau and vicinity within the framework of the larger Jemez volcanic field. The primary objective is to provide time-stratigraphic markers and geochemical information on the different volcanic rocks of the area and to identify source centers for the flows exposed along both sides of White Rock Canyon and the adjacent areas.

## SAMPLE COLLECTION, DESCRIPTION AND ANALYTICAL METHODS

Fourty six lava and dike samples were collected along the Rio Grande River in the White Rock Canyon region near Los Alamos, New Mexico (Fig. 1). The steep tributary canyons east and west of the Rio Grande provided excellent outcrops where the relative stratigraphic positions for individual samples could generally be easily determined. The flows generally exhibit a microporphyritic texture with some samples showing ophitic and granular features. Visual and optical inspection of the lava flows reveals a modal mineralogy consisting mostly of olivine, plagioclase, clinopyroxene, opaques with minor apatite phenocrysts. These minerals are also present in the groundmass and olivine is partially iddingsitized in most of the samples. Quartz xenocrysts are apparent in most of the samples collected from the flows in the northern part of White Rock Canyon Samples

Twenty samples were selected for $^{40}Ar/^{39}Ar$ dating. Most of the dated samples have relative age determinations based on mapped stratigraphic positions or crosscutting relationships. Hand samples of unaltered rocks were crushed and sieved. The 20-30 mesh fraction was ultrasonically cleaned in dilute nitric acid followed by repeated washing in distilled water. Groundmass concentrates were obtained by hand-picking whole rock fragments which were free of phenocrysts

and/or xenocrysts. Approximately 50 mg splits were wrapped in Sn-foil, encapsulated in evacuated quartz tubes and irradiated in two separate packages in the L-67 position at the University of Michigan Ford Reactor. Fish Canyon sanidine (27.84 Ma) standard was placed at ~0.5 cm intervals within the irradiation tubes in order to monitor the neutron dose and thus provide J-factors for the unknown samples. The J-factors were determined from the pooled results of 4 single crystal analyses from each flux monitor position. The J-factor error was determined to approximately ±0.5% (2 $\sigma$) and this uncertainty has been included in the total error reported for each individual age. All errors are reported at the 2$\sigma$ confidence level. Uncertainties in total gas ages are calculated by weighting the error of each step by the percent $^{39}Ar$ released. Correction factors for interfering reactions on K and Ca were determined from analysis of $K_2SO_4$ glass and $CaF_2$. Gas extraction and mass spectrometer procedures follow those outlined by McIntosh and Cather (1994).

The major and trace element compositions of bulk powders were analyzed at the Geology/Geochemistry Group XRF laboratory, Los Alamos National Laboratory using a Rigaku 3064 wavelength dispersive X-ray fluorescence (XRF) and concentrations were calculated from intensities using XRF-11 software (Criss, 1985). Analysis and statistics of the unknown samples are based on a model that uses intensities for 21 rock standards. Accuracy of results for unknowns was determined by evaluating the analytical total of all concentrations, including trace elements as oxides and the loss on ignition.

## $^{40}Ar/^{39}Ar$ RESULTS AND AGE SPECTRA INTERPRETATION

All of the whole rock samples were analyzed with the incremental heating technique and the $^{40}Ar/^{39}Ar$ isotopic results are given in Table 1. Age spectra, K/Ca, and percent $^{40}Ar$ radiogenic yield are plotted in Figure 2. All age determinations (*i.e.* total gas, plateau and/or isochron ages) are summarized in Table 1 and dates shown in bold type represent the interpreted best date for a given sample. Isochron ages are determined using the regression technique of York (1969). As indicated

by the relatively high MSWD values (*i.e.* >2.5), most of the samples do not display true isochronous behavior. Despite the high MSWD values, apparent isochron ages are generally indistinguishable from plateau and/or total gas ages and also suggest initial $^{40}Ar/^{36}Ar$ values equal to atmospheric argon (Table 1). For many of the samples, plateau ages are obtained as 3 or more contiguous heating steps, comprising greater than 50% of the total $^{39}Ar$ overlap at the $2\sigma$ level. The plateau ages and errors are calculated by weighting individual steps by the inverse of their variance.

**(insert Table 1 and Figure 2 here)**

The age spectra (Fig. 2) for the samples from this study can be categorized into four basic types:

Type 1 Flat age spectra: Samples such as DN93-14 and DN85-145a, (Fig. 2d, q) represent this type, where nearly all heating steps yield concordant apparent ages and thus give precise plateau ages. Sample DN93-13 (Fig. 2 c) yields a plateau age but the individual ages have very large errors due mainly to the low radiogenic gas yield for this analysis. The date of 3.18±0.38 Ma for this sample is considered unreliable, and thus, should not be used to constrain rigorous geologic interpretations.

Type 2 Slightly disturbed age spectra: Samples DN85-122 and DN85-147c (Fig 2n, t) show slight discordance in apparent age and either yield plateau ages comprising only about 50-75% of the total $^{39}Ar$ or do not rigorously meet the plateau criteria outlined above. For the type 2 samples meeting the plateau criteria, the plateau ages are the preferred ages (*e.g.* DN85-147c). In the case where the sample fails the plateau criteria, an age was calculated for the steps which represent the flattest portion of the age spectrum (*e.g.* DN85-122) and are denoted with quotation marks in Table 1 and Figure 2. This approach can be justified as the definition of the plateau is not completely rigorous or objective. Samples in this group probably have slightly disturbed age spectra due to a combination of minor alteration, incomplete removal of reactive gases prior to gas analysis in the mass spectrometer, non atmospheric and/or heterogeneous initial $^{40}Ar/^{36}Ar$ ratios and $^{39}Ar$ recoil.

Type 3 Disturbed age spectra with decreasing ages: Samples DN93-5 and SLR 93-1 (Fig. 2a, k) are excellent examples of this behavior as the initial heating steps yield apparent ages greater than the later increments. Some of these spectra could be showing the effect of $^{39}Ar$ recoil redistribution (Turner and Cadogan, 1974). Due to the moderate recoil energy (~175 keV) associated with the formation of $^{39}Ar$ from $^{39}K$ in the nuclear reactor, it is possible to displace a $^{39}Ar$ atom from a relatively high K (*e.g.* plagioclase, matrix, glass) into a relatively low K (*e.g.* pyroxene) site. Upon the early degassing of the plagioclase in the age spectrum experiment, anomalously high apparent ages will occur due to the depletion of $^{39}Ar_r$ and concomitantly, upon the late degassing of the pyroxene in the age spectrum experiment, anomalously low ages will occur due to the implantation of $^{39}Ar$. The observation that the K/Ca ratio generally decreases during the final degassing stages of the age spectrum experiment (Fig. 2) lends support to high K sites preferentially degassing relative to low K sites. An exception to this is sample DN93-5 (Fig. 2a) which reveals an overall decreasing age profile coupled with an overall increase in K/Ca. This results suggest that a $^{39}Ar$ recoil model can not be universally invoked to explain age spectra of this type. The type 3 spectra can not be interpreted with an explanation which requires simple excess argon contamination as isochron results are highly scattered (Table 1). Preferred ages are calculated for the flattest portions of the age spectra (Fig. 2) using the "plateau" technique.

Type 4: Disturbed age spectra with increasing ages: Apparent ages which rise during the initial incremental heating steps are evident for three samples DN85-40,129, 141 (Figs. 2m, o, p). The main reason for the relatively young initial ages in some age spectra is related to incomplete removal of reactive gases prior to mass spectrometer analysis of the argon. Poorly cleaned gas produces high pressure in the mass spectrometer, which may depress the apparent signal of the measured argon isotopes. Suppression of the $^{40}Ar$ beam due to high pressure coupled with additional gas cleanup, occurring simultaneous with gas analysis, yields anomalously low intensity values for mass 40. Also associated with this is the potential overestimation of $^{36}Ar$. Interferences occurring at mass 36 (e.g. HCl) will result in an overcorrection of the atmospheric $^{40}Ar$ component, and thus an overcorrection to an anomalously young apparent age. Fortunately, the

time versus peak-height regression of the raw intensity data yield arrays which identify which steps are affected by inadequate gas cleanup. Thus, we choose to ignore anomalously young steps which show evidence for peak height suppression and report ages for the samples based on gas increaments which have be adequately scrubbed of reactive gases. Preferred ages for these samples are calculated with either "plateau" or isochron techniques (Fig. 2, Table 1).

An exception to the above explanation for initial young ages is Sample DN85-141 (Fig. 2p). This sample appears to yield a true age gradient as the young initial steps do not have associated raw data indicative of poorly cleaned gas. This sample may have suffered argon loss associated with alteration (Foland et al., 1993) and thus we rely on the final 5 heating increments to best estimate the eruption age (Fig. 2p).

The $^{40}Ar/^{39}Ar$ results indicate three distinct age groups. The oldest age group is represented by the 9.30±0.20 Ma date given by sample SLR93-1 (Fig. 2k). Two younger age groups (2.8, 2.6-2.3 Ma) are identified when the individual preferred ages are plotted on the probability diagram shown in Figure 3. As discussed below, the youngest age group can be divided into geochemically distinct 2.6-2.4 Ma and 2.5-2.3 Ma subgroups. **(insert Figure 3 here)**

## GEOCHEMICAL RESULTS

Whole rock geochemical analysis for both major and minor trace elements were completed on 46 samples (Fig. 1, Table 2). Despite temporal similarities and spatial proximity, the samples from volcanic flows, centers, and dikes exposed along both walls and shoulders of White Rock Canyon display a range of major- and trace-element compositions (Table 2, Fig. 4). These samples generally exhibit compositional ranges (e.g., $SiO_2$ = 49.07-58.42 wt % and MgO = 1.93-7.33 wt %) and show well-defined trends with a number of off-trend points (Fig. 4). On the silica-total alkali diagram of Le Bas et al. (1986), these lava flows plot in the basaltic (tholeiitic), hawaiite (trachybasalt), mugearite (basaltic trachyandesite), benmorite (trachyandesite), and dacite fields (Fig. 5). Binary plots of trace elements and trace-element ratios also show the same kind of geochemical trends as shown by the major elements (Figs. 6a and b).**(insert Table 2, Figs. 4,5, 6)**

The geochemical composition with respect to sample location, along with sample stratigraphic position and $^{40}Ar/^{39}Ar$ age are shown schematically in Figure 1. The general observation drawn from Figure 1 is that consistent patterns within the geochemically diverse rock types are present at different sections along the traverse. For example, tholeiite lavas generally overlay mugearite and/or hawaiite outcrops (Fig. 1). An exception to this is the sequence found at Caja del Rio canyon. Here a thick tholeiite lava-lake, ponded inside the Caja del Rio maar, occurs stratigraphically below the hawaiite flows (Fig. 1). In detail, many of the mugearite samples have distinct geochemical signatures and thus can not be universally grouped (Table 2). Three mugearite samples (DN85-4, 137 and SLR93-1) occurring west of the Rio Grande at Water and Ancho Canyons are additionally distinct as they have high $Al_2O_3$ (18.2-19.1 wt%) and low MgO (1.8-2.3 wt%) relative to the other mugearite samples (Table 2). Hawaiite lavas occur sporadically throughout the study area and are generally found in the basal portions of a given stratigraphic succession (Fig. 1). Three chemically identical benmorite lavas were sampled west of the Rio Grande, and like the mugearites and hawaiites, occur low in the stratigraphic sequence (Fig. 1).

Some geochemical patterns with respect to geographic location are apparent. Outcrops of tholeiitic composition are confined to the Pajarito Plateau , extending as far east as White Rock Canyon. Outcrops of more evolved rocks such as hawaiite, mugearite, benmorite, and dacite are restricted to the Cerros del Rio area and the immediate vicinity of White Rock Canyon (Fig. 1).

## DISCUSSION

### Chronology of volcanism and temporal geochemical trends

Lavas and dikes exposed in the White Rock Canyon area and the Pajarito Plateau erupted episodically in the late Miocene and Pliocene periods (Fig. 3). These rocks display a range of major and trace element compositions and can be divided into temporally and geochemically distinct eruptive pulses: 9.3 Ma mugearite, 2.8 Ma benmorite and tholeiite, 2.6-2.4 Ma mugearite and hawaiite, and 2.5-2.3 Ma tholeiite (Fig. 3). The eruption centers for most of these rocks are

buried, but the possible location of some centers can be inferred by combining geochemical and age data with field relationships.

The 9.3 Ma late Miocene pulse is defined by a single sample (SLR-93-1) dated at 9.30±0.20 Ma, collected from a high $Al_2O_3$-low MgO (Table 2) mugearite exposed at the base of the sequence in Ancho Canyon (Figs. 1, 2). This sample differs from a nearby high Al-low Mg mugearite (DN85-4) as it contains higher Cr and Ni and lower Ba and Sr (Table 2).

The 2.8 Ma Pliocene pulse is defined by a benmorite (F93-FRIJ-6) from Frijoles Canyon and a tholeiite (DN85-129) from the basal section at Chaquehui Canyon, both located in the southern portion of the study area (Fig. 1). This older tholeiite occurs within a phreatomagmatic sequence and is apparently derived from a nearby source. This tholeiite has a distinct trace element composition relative to younger 2.5-2.3 Ma tholeiites. The 2.8 Ma benmorite is probably stratigraphically below the DN85-129 tholeiite and is chemically identical to the undated benmorites which occur stratigraphically low at Water and Ancho Canyons (Fig. 1).

The majority of the dated samples fall within a narrow time range between 2.6 to 2.3 Ma (Fig. 3). This time window can be further subdivided into a 2.3-2.5 Ma tholeiitic group and a 2.4-2.6 hawaiite/mugearite group (Fig. 3). The resolution of the age data cannot alone distinguish whether the temporal overlap of the two groups is apparent or real. However, the stratigraphically consistent relationships of thoeiites overlying evolved rocks suggests that these eruptions did not overlap in time.

The 2.6-2.4 Ma pulse includes both mugearite and hawaiite compositions. The mugearites display a range of compositions, but only temporal or spatial trends are apparent. The mugearites exposed along both sides of the northern end of White Rock Canyon (Fig. 1) are similar in composition and appear to have erupted and flowed westward from the Buckman Mesa maar. The undated mugearite samples northeast of Cochiti Dam have similar major and trace element compositions to the northern White Rock Canyon rocks and probably erupted from the southwest side of the Cerros del Rio volcanic field.

Like the mugearite samples, the 2.4-2.6 hawaiites can not all be geochemically linked. Sample DN93-25 from the southern end of White Rock Canyon is different in composition to the three more northerly located hawaiites. Two of the hawaiite samples (DN85-122 and DN86-1a) are indistinguishable in age at the 2σ level (Fig. 1) and appear to represent a single 2.5 Ma lava which flowed locally westward near the present canyon. A somewhat older (2.54 Ma) hawaiite flow occurs at the base of the eastern wall of White Rock Canyon. It is suggested that these lavas were erupted and flowed generally northward from vents in the Cerros del Rio volcanic field (Aubele, 1979). A geochemically distinct hawaiite (DN93-25) yields a somewhat problematic preferred isochron age of 2.39±0.08 Ma. This sample is cut by a mugearite dike (DN93-26) which is precisely dated at 2.54±0.02 Ma (Fig. 1). The high MSWD of 7.3 (Table 1) for the isochron array of sample DN93-25 may be indicative of nonhomogeneous trapped initial argon components and thus suggests caution in the use of the isochron age. We note that the total gas and "plateau" ages (~2.51 Ma, Table 1) for DN93-25 are indistinguishable from DN93-26 and may provide a more reliable estimate for the eruption age of this chemically distinct hawaiite.

The 2.3-2.5 Ma basalt flows of tholeiitic composition occur along the western side of White Rock Canyon and consistently stratigraphically overlie the mugearite/hawaiite flows (Fig. 1). These tholeiitic lavas flowed east or south-southeast into an ancestral lake in White Rock Canyon as indicated by the occurrence of pillow lavas. Other tholeiite lavas from central and southern parts of White Rock Canyon yielded similar isotopic ages (Fig. 1) and appear to have erupted along a fissure east of and parallel to the Pajarito fault zone.

In addition to the dated units summarized above, mugearite and dacite lavas have been identified at the southern part of White Rock Canyon (Fig. 1), but have not yet been dated.

## Relationship to regional volcanism and tectonism

The dated sequence of Miocene and Pliocene volcanic rocks described in the previous section can be compared to other known volcanic and tectonic events in this part of the Rio Grande rift. The oldest mugearite flow (9.30 Ma), exposed east of the Pajarito fault zone, erupted during

intense late Miocene (10-7 Ma) magmatic and tectonic activities related to the voluminous and temporally correlative igneous activity, including the Paliza Canyon Formation and the Lobato Basalt of southern and northern Jemez volcanic field, respectively, and dike intrusions in the northwestern Española basin (Baldridge et al., 1980; Gardner et al., 1986; Goff et al., 1989; Aldrich and Dethier, 1990). However, the late Miocene mugearite flow is distinct in its major and trace element compositions compared with the volcanic rocks of the Jemez volcanic field.

The late Pliocene episode was dominated by diverse volcanic rocks of relatively mafic composition. These volcanic rocks erupted within the rift basin east of the Pajarito fault zone of the Jemez volcanic field. The $^{40}Ar/^{39}Ar$ results (2.77-2.33 Ma) are similar to, but much more precise than, published K/Ar ages from the White Rock Canyon and the Cerros del Rio volcanic field (Manley, 1976; Bachman and Mehnert, 1978) except for an older K/Ar age (4.4 Ma) from the eroded volcanic center and maar (Black Mesa at San Ildefonso) at the northern part of the volcanic field (Baldridge et al., 1980). Other basaltic eruptions with similar K/Ar ages have been identified throughout the rift basin to the north (El Alto) and south (Santa Ana Mesa) of the Cerros del Rio volcanic field (Baldridge et al., 1980; Manley and Mehnert, 1981; Goff et al., 1989). The prevalence of rift-bound volcanic eruptions in the northern part of the Rio Grande rift during the late Pliocene time may be related to early Pliocene intense faulting that resulted in the formation of the Pajarito fault zone (Manley, 1979) and to the formation of hybrid magma chambers within the crust under the Jemez volcanic field that caused the rift-ward migration of the dense mafic magmas and the rift margin (Gardner and Goff, 1984). The dense mafic magmas could not ascend through voluminous silicic magmas that ultimately erupted to form the Plio-Pleistocene pyroclastic rocks of the Jemez volcanic field.

## Geochemical evolution of volcanic rocks

Despite temporal similarities and geographic proximity, the volcanic rocks of White Rock Canyon and the Pajarito Plateau exhibit a relatively wide compositional range. This geochemical diversity may be attributed to some combination of heterogeneous mantle source, fractional crystallization, and crustal contamination during ascent (Aubele, 1979; Duncker et al., 1991;

Baldridge et al., 1995). Rocks of alkaline affinity containing xenocrystic quartz and lavas of tholeiitic and hawaiite compositions contaminated by crustal materials were described from the Cerros del Rio volcanic field (Duncker et al., 1991). Huppert and Sparks (1985) suggested that a $K_2O$ versus Ni plot can be used to assess the degree of crustal contamination of basaltic magma because the contaminated rocks plot as scattered data points along mixing lines away from the fractionation trend. However, Kerr et al.(1995) argued that the same trend can be produced by mixing genetically-related basaltic and evolved magmas. Instead, a plot of Zr versus Ni was suggested to evaluate the extent of crustal contamination because Zr concentration is minimal in crustal rocks, whereas its concentration is higher in evolved magmas (Kerr et al., 1995). A plot of Zr versus Ni of the samples indicates a possible fractionation trend from high Ni to low Zr with numerous off-trend data points that probably represent contaminated flows (Fig. 6c). According to Metcalf (1995), magmatic sources could be assessed by plotting Nb/Y versus MgO because the ratio is insensitive to fractionation, whereas MgO is affected by it. A plot of the White Rock Canyon samples (Fig. 6d) shows a narrow range of Nb/Y ratio for the White Rock Canyon samples, although these values might have been modified by contamination. Kerr et al. (1995) suggested that crustal contamination can occur by partial melting and assimilation during turbulent ascent of magma. In many cases, the most evolved rocks are the initial flows and subsequent rocks becoming less evolved. Except for the earliest tholeiitic flow in Chaquehui Canyon, the late Pliocene stratigraphic sequence is represented by basal benmorite, mugearite, and hawaiite, overlain by tholeiitic flows. This compositional trend with time may reflect variation in crust/mantle magma sources and fractionation history. It may also be related to the effects of the initial flow that created a chilled margin around the conduit thereby shielding subsequent magmas from crustal contamination.

## CONCLUSION

Rift-bounded late Miocene and Pliocene volcanic rocks are exposed east of the present-day Pajarito fault zone along White Rock Canyon, the eastern edge of the Pajarito Plateau, and the

western Cerros del Rio volcanic field. In these areas, the volcanic rocks consist mainly of tholeiite, hawaiite, mugearite, benmorite, and dacite lava flows. In most of the exposed sections along White Rock Canyon, the tholeiitic lavas occur as uppermost flows, whereas the underlying flows are compositionally more evolved.

The oldest lava (9.30 Ma) is exposed locally in White Rock Canyon, whereas the younger late Pliocene (2.8-2.3 Ma) activity was voluminous, widespread, and compositionally diverse. These late Pliocene volcanic rocks are similar to other mafic volcanic fields peripheral to the Jemez volcanic field and appear to be temporally related to the formation of the Pajarito fault zone that marks the western margin of the Española Basin. Within the episode of late Pliocene activity, older (2.8-2.4 Ma) lavas and dikes are relatively evolved, reflecting at least some crustal contamination. The younger (2.5-2.3 Ma) tholeiite lavas show minimal crustal input, possibly because extension along active faults or fractures provided a path for rapid magmatic ascent.

## ACKNOWLEDGMENTS

This work was supported by the Los Alamos National Laboratory Environmental Restoration Project. DPD was supported by the Associated Western Universities and by the Bronfman Science Center, Williams College. The generous permission granted by the San Ildefonso Pueblo to conduct studies on tribal land is greatly acknowledged. Constructive reviews by Scott W. Baldridge, Grant Heiken, Yemane Asmerom, and Bill McIntosh is gratefully acknowledged for improving the manuscript's organization and scientific clarity.

## REFERENCES

Aldrich, M. J., Jr. and Dethier, D. P. 1990, Stratigraphic and tectonic evolution of the northern Española basin, Rio Grande rift, New Mexico: Geological Society of America Bulletin, v. 102, p. 1695-1705.

Aubele, J. C., 1979, The Cerros del Rio volcanic field: New Mexico Geological Society, Guidebook 30, p. 243-252.

Bachman, G. O. and Mehnert, H. H., 1978, New K-Ar dates and the late Pliocene to Holocene geomorphic history of the central Rio Grande region, New Mexico: Geological Society of America Bulletin, v. 89, p. 283-292.

Baldridge, W. S., Keller, G. R., Haak, V., Wendlandt, E., Jiracek, G. R., and Olsen, K. H., 1995, The Rio Grande Rift: in Olsen, K. H., ed., Continental Rifts: Evolution, Structure, Tectonics: Amesterdam, Elsevier, p. 233-275.

Baldridge, W. S., Damon, P. E., Shafiqullah, M., Bridwell, R. J., 1980, Evolution of the central Rio Grande rift : new potassium-argon ages: Earth Planetary Science Letters, v. 51, p. 309-321.

Baldridge, W. S., 1979, Petrology and petrogenesis Plio-Pleistocene basaltic rocks from the central Rio Grande Rift : in Riecker, R. E., ed., Rio Grande Rift: Tectonics and Magmatism, American Geophysical Union, Washington D. C., p. 323-353.

Budding , A. J., 1978, Subsurface geology of the Pajarito Plateau: interpretation of gravity data: in Hawley, J. W., ed., Guidebook to the Rio Grande Rift in New Mexico and Colorado, New Mexico Bureau of Mines and Mineral Resources Circular 163, p. 196-198.

Criss, J., 1985, User's Guide to XRF-11 Software for Fundamental Parameters: Criss Software Inc. Largo, MD, v.15, 49 p.

Dethier, D. P. (in press), Geologic map of the White Rock quadrangle, New Mexico Bureau of Mines and Mineral Resources.

Duncker, K. E., Wolff, J. A., Harmon, R. S., Leat P. T., Dickin, A. P., and Thompson, R. N., 1991, Diverse mantle and crustal components in lavas of the NW Cerros del Rio volcanic field, Rio Grande rift, New Mexico: Contributions Mineralogy and Petrology, v. 108, p. 331-345.

Ferguson, J. F., Baldridge, W. S., Brail, L.W., Biehler, S., Gilpin, B., and Jiracek, G.R. 1995, Structure of the Española Basin, Rio Grande Rift, New Mexico, from SAGE seismic and gravity data: New Mexico Geological Society , Guidebook 46, p. 105-110.

Foland, K. A., Fleming, T. H., Heimann, A., and Elliot, D. H., 1993, Potassium-argon dating of fine-grained basalts with massive Ar loss: Application of the 40Ar/39Ar technique to plagioclase and glass from the Kirkpatrick Basalt, Antarctica: Chemical Geology, v. 107, p. 173-190.

Gardner , J. N., Goff, F., Garcia, S., and Hagan, R. C., 1986, Stratigraphic relations and lithologic variations in the Jemez volcanic field, New Mexico: Journal of Geophysical Research, v. 91, p. 1763-1778.

Gardner, J. N. and Goff, F., 1984, Potassium-argon dates from the Jemez volcanic field: implications for tectonic activity in the north-central Rio Grande rift: New Mexico Geological Society, Guidebook 35, p. 75-81.

Goff, F., Gardner, J. N., Baldridge, W. S., Hulen, J. B., Nielson, D. L., Vaniman, D., Heiken, G., Dungan, M. A., Broxton, D., 1989, Volcanic and hydrothermal evolution of Valles caldera and Jemez volcanic Field: in Chapin, C. E. and Zidek, J., eds., Field Excursions to Volcanic Terranes in the Western United States, V. I: Southern Rocky Mountain Region: New Mexico Bureau of Mines and Mineral Resources, Memoir 46, p. 381-434.

Golombeck, M. P., 1983, Geology, structure, and tectonics of the Pajarito fault zone in the Española Basin of the Rio Grande rift, New Mexico: Geological Society of America Bulletin, v. 94, p. 192-205.

Huppert, H. E. and Sparks, R. S. J., 1985, Cooling and contamination of mafic and ultramafic magmas during ascent through continental crust: Earth Planetary Science Letters, v. 74, p. 371-386.

Izett, G. A. and Obradovich, J. D., 1994, 40Ar/39A4 age constraints for the Jaramillo normal subchron and the Matuyama-Brunhes geomagnetic boundary: Journal of Geophysical Research, v. 99, p. 2925-2934.

Kerr, , A. C., Kempton, P. D., Thompson, R. N., 1995, Crustal assimilation during turbulent magma ascent (ATA); new isotopic evidence from the Mull Tertiary lava succession, N. W. Scotland: Contributions Mineralogy and Petrology, v. 119, p. 142-154.

Le Bas, M. J., Le Maitre, R. W., Streckeisen, A., and Zanettin, B., 1986, A chemical classification of volcanic rocks based on the total alkali-silica diagram: Journal of Petrology, v. 27, p. 745-750.

Manley, K., 1979, Stratigraphy and structure of the Española Basin, Rio Grande rift, New Mexico: in Riecker, R. E. ed., Rio Grande Rift: Tectonics and Magmatism, American Geophysical Union, Washington D. C., p. 71-86.

Manley, K., 1976, K-Ar age determinations of Pliocene basalts from the Esapñola Basin , New Mexico: Isochron West, v. 16, p. 29-30.

Manley, K. and Mehnert, H. H., 1981, New K-Ar ages of Miocene and Pliocene volcanic rocks in the northwestern Esapñola Basin, and their relationship to the history of the Río Grande rift: Isochron West, v. 30, p. 5-8.

McIntosh, W.C., and Cather, S.M., 1994, 40Ar/39Ar geochronology of basaltic rocks and constraints on Late Cenozoic stratigraphy and landscape development in the Red Hill-Quemado area, New Mexico: New Mexico Geological Society Guidebook, v. 45, p. 209-224.

Metcalf, R.V., 1995, Proterozoic plutonic rocks of the central Santa Fe Range: trace element evidence of subduction zone magmatism, north central New Mexico: New Mexico Geological Society , Guidebook 46, p. 185-192.

Reneau, S.L., Dethier, D. P., and Carney, J. S., 1995, Landslides and other mass movements near Technical Area 33, Los Alamos National Laboratory: Los Alamos Report LA-12955-MS, 48 p.

Turner, G. and Cadogan, P. H., 1974, Possible effects of 39Ar recoil in 40Ar/39Ar datingof lunar samples: Geochimica et Cosmochimica Acta, v. 5, p. 1601-1615.

York, D., 1969, Least squares fitting of a straight line with correlated errors: Earth Planetary Science Letters v. 5, p. 320-324.

Table captions

Table 1. Summary of $^{40}Ar/^{39}Ar$ ages. Ages in **bold** type are interpreted to be the best measure of the eruption age of the samples. Plateau ages designated with quotation marks do not rigorously meet the defined plateau criteria and represent ages calculated using the inverse of the variance for the steps indicated on the age spectra figures. The type of age spectrum listed in the comments refer to the type definitions discussed in the argon results section. B=benmorite, H=hawaiite, M=mugearite, T=tholeiite.

Table 2. Major and trace element analyses of volcanic rocks from White Rock Canyon, the Pajarito Plateau, and the Cerro del Rio volcanic field, New Mexico.

Figure captions

Figure 1. Location map of samples in White Rock Canyon, the Pajarito Plateau, and the Cerro del Rio volcanic field, New Mexico. The inset maps show the location of the study area with reference to the Pajarito fault zone of the Española Basin. Schematic stratigraphic sections for various locations along with sample number, geochemical classification and $^{40}Ar/^{39}Ar$ age are also shown.

Figure 2. $^{40}Ar/^{39}Ar$ age spectra for step-heating experiments on whole-rock basaltic rocks from White Rock Canyon, Pajarito Plateau, Cerros del Rio volcanic field, Jemez volcanic field, New Mexico. All errors shown are reported at the $2\sigma$ confidence level.

Figure 3. Probability diagram of the preferred ages listed in Table 1. Individual ages and errors ($2\sigma$) are shown along with sample number and composition. The age distribution clearly shows distinct age pulses which are consistent with geochemical groupings and stratigraphic relationships.

Figure 4. Variation diagrams of major elements (wt %) versus $SiO_2$. Analysis calculated to 100 % volatile free. Symbols represent sample locations from the west (solid circle) and east (open square) sides of the White Rock Canyon. The late Miocene flow (solid diamond) is from the mouth of Ancho Canyon.

Figure 5. Total alkali - $SiO_2$ plot of volcanic flows from White Rock Canyon and vicinity. Main rock-type boundaries are from Le Bas et al. (1986). The symbols are as in Figure 4.

Figure 6. Variation diagram of selected trace elements and trace-element ratios of samples. The symbols are the same as in Figure 3.

| Sample | Isochron age (Ma) | $^{40}Ar/^{36}Ar_i$ | Isocrhon MSWD | Isochron steps | Total gas age (Ma) | Plateau age (Ma) | %$^{39}$Ar in plateau | Comments |
|---|---|---|---|---|---|---|---|---|
| DN93-5T | 2.45±0.02 | 295.6+3.8 | 24.0 | all | 2.46±.06 | "2.45±0.06" | 100 | Ages decrease from initial to ending steps, K/Ca increases, (type 3) |
| DN93-8M | 2.30±0.6 | 299.8+9.4 | 2.7 | all | 2.68±0.22 | 2.59±0.18 | 100 | Flat age spectrum, (type 1) |
| DN93-13T | 2.90±0.6 | 296.5+5.6 | 0.3 | all | 3.2+0.8 | 3.18±0.38 | 100 | Flat age spectrum, high error reflects low radiogenic yield, (type 1) |
| DN93-14M | 2.47±0.06 | 297.6±4.0 | 3.4 | all | 2.51±0.08 | 2.50±0.04 | 100 | Flat age spectrum (type 1) |
| DN93-21T | 2.31±0.08 | 297.1±5.0 | 5.5 | b-d | 2.27+..12 | 2.33±0.08 | 89 | Last 3 steps anomalously young, potentially due to $^{39}$Ar recoil, (type 2) |
| DN93-25H | 2.39±.0.08 | 300.2+3.4 | 7.3 | c-g | 2.51±0.14 | "2.49±0.12" | 95 | Complex age spectrum, (type 2) |
| DN93-26M | 2.55±0.02 | 289.0±3.2 | 3.6 | all | 2.52±0.03 | 2.54±0.02 | 64 | Flat age spectrum, highly radiogenic, (type 1) |
| DN93-27T | 2.48±0.06 | 295.4±3.0 | 9.6 | all | 2.45±0.14 | "2.48±0.12" | 76 | Disturbed age spectrum (type 2) |
| DN93-28T | 2.45±0.06 | 287.6±4.1 | 0.2 | all | 2.27±0.12 | 2.36±0.06 | 68 | Slightly disturbed age spectrum (type 2) |
| F93-FRIJ-6B | 2.77±0.02 | 287.2±5.0 | 99.0 | b-h | 2.67±0.08 | "2.75±0.08" | 90 | Complex age spectrum (type 3 and 4)) |
| SLR 93-1M | 9.33±0.06 | 289.6±3.0 | 138.0 | b-h | 9.12±0.16 | "9.30±0.20" | 94 | Complex age spectrum (type 3 and 4) |
| DN86-1aH/M | 2.47±0.02 | 287.1±4.8 | 6.5 | c-h | 2.47±0.08 | 2.46±0.02 | 93 | Flat age spectrum, highly radiogenic, (type 1) |
| DN85-145aM | 2.57±0.02 | 295.6±2.0 | 1.8 | all | 2.54±0.24 | 2.57±0.02 | 100 | Flat age spectrum, highly radiogenic, (type 1) |
| DN85-145cM | 2.54±0.02 | 303.3±4.4 | 18.0 | all | 2.54±0.04 | 2.55±0.02 | 91 | Flat age spectrum, highly radiogenic, (type 1) |
| DN85-147bM | 2.49±0.02 | 294.8±4.0 | 10.0 | all | 2.48±0.08 | 2.50±0.02 | 77 | Slightly disturbed age spectrum (type 2) |
| DN85-147cT | 2.49±0.03 | 286.3±3.0 | 7.6 | all | 2.37±0.08 | 2.46±0.03 | 53 | Slightly disturbed age spectrum (type 2) |
| DN85-40H | 2.52±0.04 | 297.6±3.2 | 6.4 | f-i | 2.39±0.34 | "2.54±0.06" | 82 | Steps a-e not completely cleaned of reactive gases, (type 4) |
| DN85-141T | 2.39±0.08 | 296.4±6.4 | 3.1 | e-i | 2.08±0.14 | "2.40±0.06" | 43 | Age gradient possibly related to alteration, (type 4) |
| DN85-129T | 2.85±0.17 | 290±14 | 0.4 | g-i | 2.2±1.0 | 2.78±0.04 | 77 | Steps a-f not completely cleaned of reactive gases, (type 4) |
| DN85-122H | 2.48±0.02 | 308.0±3.2 | 20.7 | all | 2.54±0.04 | "2.49±0.03" | 90 | Slightly disturbed age spectrum (type 2) |

| Sample Number | AWL19-93 | D85-40 | DN85-69A | DN85-69B | DN85-72A | DN85-72B | DN85-72C | DN85-126 | DN85-129 | DN85-131 | DN85-137 |
|---|---|---|---|---|---|---|---|---|---|---|---|
| SIO2 | 50.74 | 49.79 | 55.42 | 57.28 | 47.99 | 52.92 | 51.61 | 49.5 | 49.29 | 50.03 | 55.06 |
| TIO2 | 1.5 | 1.61 | 1.7 | 1.24 | 1.71 | 1.58 | 1.7 | 1.47 | 1.44 | 1.49 | 1.46 |
| Al2O3 | 16.25 | 16.59 | 16.28 | 16.19 | 13.83 | 14.73 | 16.23 | 16.87 | 16.12 | 16.38 | 18.08 |
| Fe2O3 | 11.39 | 9.63 | 10.25 | 8.37 | 9.42 | 9.57 | 9.62 | 10.78 | 11.14 | 11.89 | 8.36 |
| MnO | 0.16 | 0.14 | 0.14 | 0.12 | 0.15 | 0.22 | 0.14 | 0.16 | 0.16 | 0.18 | 0.08 |
| MgO | 6.86 | 6.3 | 3.75 | 4.93 | 5.89 | 6.97 | 6.16 | 6.26 | 7.33 | 6.75 | 2.31 |
| CaO | 9.04 | 8.59 | 7.05 | 6.93 | 9.31 | 7.37 | 8.6 | 9.53 | 9.94 | 9.34 | 6.72 |
| Na2O | 3.2 | 3.7 | 4.12 | 3.8 | 3 | 3.53 | 3.6 | 3.49 | 3.26 | 3.42 | 4.47 |
| K2O | 1.08 | 1.75 | 1.69 | 2.01 | 1.92 | 2.28 | 1.85 | 1.1 | 0.88 | 0.88 | 2.15 |
| P2O5 | 0.31 | 0.76 | 0.61 | 0.41 | 0.83 | 0.6 | 0.7 | 0.51 | 0.48 | 0.34 | 0.62 |
| Total | 100.53 | 98.86 | 101 | 101.27 | 94.06 | 99.76 | 100.21 | 99.66 | 100.05 | 100.7 | 99.31 |
| V | 178.58 | 174.16 | 162.81 | 129.43 | 189.93 | 172.33 | 158.93 | 191.84 | 192.11 | 186.81 | 174.03 |
| Cr | 219.99 | 103.32 | 34.08 | 109.82 | 128.57 | 186.18 | 178.11 | 78.69 | 192.68 | 190.29 | 58.16 |
| Ni | 92.25 | 63.57 | 16.97 | 69.31 | 77.79 | 120.15 | 103.57 | 54.06 | 83.21 | 98.62 | 34.97 |
| Zn | 89.1 | 86.93 | 96.73 | 89.9 | 83.07 | 79.21 | 76 | 83.39 | 72.22 | 100.66 | 77.93 |
| Pb | 16.73 | 23.96 | 25.51 | 26.24 | 29.35 | 33.65 | 24.69 | 18.11 | 12.71 | 10.79 | 30.18 |
| SR | 438.27 | 1227.81 | 656.35 | 804.5 | 1063.76 | 765.94 | 1019.79 | 678.85 | 652.55 | 454 | 1146.63 |
| Y | 26.22 | 24.73 | 31.1 | 21.42 | 29.37 | 22.36 | 23.31 | 25.83 | 20.32 | 29.37 | 23.7 |
| Zr | 143.25 | 251.18 | 225.42 | 191.59 | 233.05 | 194.77 | 215.13 | 161.68 | 152.72 | 147.62 | 268.8 |
| Nb | 18.39 | 44.76 | 29.23 | 19.72 | 40.21 | 36.99 | 38.25 | 26.71 | 25.31 | 19.3 | 34.55 |
| Ba | 436.01 | 1109.74 | 1019.27 | 1018.38 | 1365 | 1045.25 | 1479.65 | 691.01 | 515.73 | 484.92 | 1087.34 |

| | DN85-72D | DN85-100 | DN85-104 | DN85-107A | DN85-113A | DN85-122 | DN85-123B | DN85-145A | DN85-145B | DN85-145C | DN85-145F |
|---|---|---|---|---|---|---|---|---|---|---|---|
| SIO2 | 52.85 | 57.84 | 50.34 | 62.17 | 65.8 | 50.48 | 50.19 | 53.64 | 53.16 | 53.23 | 52.78 |
| TIO2 | 1.72 | 1.08 | 1.67 | 0.56 | 0.61 | 1.52 | 1.52 | 1.61 | 1.65 | 1.53 | 1.65 |
| Al2O3 | 15.12 | 16.71 | 16.87 | 15.23 | 16.09 | 16.21 | 17.24 | 15.43 | 15.73 | 15.52 | 14.94 |
| Fe2O3 | 9.35 | 7.31 | 9.63 | 4.46 | 4.58 | 9.43 | 10.86 | 9.22 | 9.06 | 8.83 | 9.32 |
| MnO | 0.15 | 0.11 | 0.15 | 0.07 | 0.08 | 0.15 | 0.15 | 0.13 | 0.15 | 0.14 | 0.14 |
| MgO | 6.06 | 3.94 | 5.43 | 2.06 | 2.21 | 6.93 | 5.57 | 6.18 | 6.21 | 6 | 6.99 |
| CaO | 7.69 | 6.55 | 7.98 | 4.71 | 4.38 | 8.7 | 9.27 | 7.73 | 7.97 | 7.8 | 7.66 |
| Na2O | 4.1 | 4.28 | 4.79 | 4.68 | 4.51 | 4.32 | 3.75 | 3.89 | 3.91 | 4.17 | 3.62 |
| K2O | 2.64 | 2.11 | 1.76 | 2.59 | 2.72 | 1.78 | 1.26 | 2.33 | 2.34 | 2.44 | 2.31 |
| P2O5 | 0.74 | 0.53 | 0.78 | 0.33 | 0.38 | 0.92 | 0.53 | 0.6 | 0.65 | 0.73 | 0.63 |
| Total | 100.41 | 100.45 | 99.39 | 96.85 | 101.35 | 100.43 | 100.35 | 100.75 | 100.81 | 100.39 | 100.05 |
| V | 180.76 | 121.27 | 187.02 | 60.5 | 67.1 | 158.19 | 204.34 | 167.77 | 173.48 | 152.27 | 188.91 |
| Cr | 148.82 | 92.03 | 78.69 | 32.16 | 33.32 | 148.69 | 69.31 | 173.94 | 171.47 | 153.55 | 182.49 |
| Ni | 90.99 | 64.28 | 53.35 | 20.12 | 19.88 | 114.02 | 55 | 102.62 | 88.87 | 104.67 | 105.45 |
| Zn | 85 | 85.64 | 84.68 | 74.8 | 74.15 | 92.07 | 101.47 | 85.88 | 85.32 | 73.11 | 51.98 |
| Pb | 40.97 | 30.82 | 26.61 | 39.87 | 43.71 | 26.52 | 20.48 | 38.12 | 34.38 | 38.31 | 33.74 |
| SR | 980.05 | 925.93 | 1127.18 | 969.9 | 832.49 | 1338.58 | 720.87 | 844.75 | 905.64 | 988.51 | 832.92 |
| Y | 24.73 | 21.26 | 23.07 | 11.97 | 19.37 | 24.33 | 26.85 | 24.73 | 25.87 | 24.1 | 23.62 |
| Zr | 235.42 | 239.64 | 258.66 | 205.21 | 231.57 | 262.68 | 172.05 | 194.11 | 209.28 | 218.83 | 201.07 |
| Nb | 46.5 | 29.72 | 45.24 | 16.43 | 21.47 | 44.69 | 26.99 | 38.39 | 40.98 | 39.79 | 38.6 |
| Ba | 1280.81 | 1203.78 | 1106.15 | 1505.62 | 1468 | 1119.59 | 876.5 | 1049.73 | 1243.19 | 1287.08 | 1038.98 |

| Sample Number | DN85-139B | DN85-140 | DN85-141 | DN86-1B | DN86-4 | DN93-5 | DN93-8 | DN93-13 | DN93-14 | DN93-21 | DN93-23 | DN93-25 |
|---|---|---|---|---|---|---|---|---|---|---|---|---|
| SiO2 | 58.78 | 51.31 | 52.04 | 51.32 | 53.69 | 51.84 | 56.28 | 52.13 | 50.2 | 51.38 | 52.18 | 49.06 |
| TiO2 | 0.95 | 1.49 | 1.51 | 1.48 | 1.46 | 1.51 | 1.15 | 1.51 | 1.66 | 1.44 | 1.15 | 1.64 |
| Al2O3 | 16.43 | 16.2 | 16.42 | 15.96 | 19.08 | 15.97 | 16.26 | 16.27 | 17.04 | 15.86 | 16.29 | 16.38 |
| Fe2O3 | 6.64 | 11.28 | 11.27 | 11.46 | 8.92 | 11.35 | 7.79 | 11.15 | 9.63 | 11.64 | 11.86 | 9.81 |
| MnO | 0.11 | 0.16 | 0.16 | 0.16 | 0.13 | 0.16 | 0.12 | 0.16 | 0.15 | 0.16 | 0.16 | 0.16 |
| MgO | 4.28 | 6.61 | 6.02 | 7.33 | 1.93 | 6.59 | 5.06 | 5.98 | 5.5 | 7.34 | 7.11 | 5.9 |
| CaO | 6.52 | 8.98 | 9.01 | 9.01 | 6.44 | 8.91 | 7.65 | 9 | 8.25 | 8.88 | 9.06 | 9.87 |
| Na2O | 4.3 | 3.18 | 3.29 | 3.16 | 5.02 | 3.41 | 4.09 | 3.33 | 4.29 | 3.24 | 3.14 | 5.02 |
| K2O | 2.1 | 1.11 | 1.14 | 1.07 | 2.33 | 1.08 | 1.86 | 0.95 | 1.75 | 0.96 | 0.39 | 0.93 |
| P2O5 | 0.51 | 0.33 | 0.32 | 0.31 | 0.95 | 0.32 | 0.55 | 0.34 | 0.81 | 0.31 | 0.13 | 1.2 |
| Total | 100.62 | 100.64 | 101.16 | 101.26 | 99.94 | 101.14 | 100.82 | 100.8 | 99.26 | 101.21 | 101.46 | 99.98 |
| V | 108.7 | 181.3 | 183.88 | 180.55 | 161.86 | 190.68 | 136.71 | 176.13 | 171.04 | 187.96 | 174.09 | 176.95 |
| Cr | 110.51 | 197.34 | 152.11 | 251.05 | 7.73 | 218.69 | 106.06 | 152.52 | 64.25 | 262.27 | 172.02 | 124.26 |
| Ni | 64.43 | 92.49 | 64.28 | 105.45 | 7.15 | 103.09 | 73.55 | 75.36 | 41.41 | 123.21 | 162.58 | 63.33 |
| Zn | 71.5 | 94.32 | 96.09 | 90.38 | 97.77 | 94.48 | 77.85 | 97.29 | 72.06 | 93.68 | 95.12 | 69.57 |
| Rb | 29.99 | 20.21 | 19.57 | 18.75 | 31.55 | 20.48 | 26.88 | 18.2 | 25.33 | 16.83 | 6.04 | 38.86 |
| SR | 900.56 | 440.47 | 421.95 | 434.38 | 1329.28 | 429.4 | 938.62 | 417.81 | 1311.53 | 430.49 | 262.47 | 1500.1 |
| Y | 19.69 | 25.12 | 27.8 | 26.22 | 24.33 | 27.4 | 25.04 | 27.8 | 24.96 | 27.4 | 18.35 | 30.08 |
| Zr | 231.86 | 148.06 | 147.1 | 141.18 | 309.67 | 151.17 | 237.64 | 149.76 | 251.18 | 140.66 | 73.36 | 277.54 |
| Nb | 26.99 | 19.65 | 18.39 | 18.32 | 50.56 | 20.56 | 27.9 | 18.67 | 42.17 | 16.5 | 9.3 | 50.14 |
| Ba | 1217.22 | 428.4 | 383.17 | 374.21 | 1480.54 | 488.59 | 1288 | 402.33 | 1000.46 | 408.25 | 177.88 | 1527.1 |

| | DN85-147B | DN85-147C | DN86-1A | DN93-27 | DN93-28 | F93FRIJ6 | SLR93-1 | DN93-26 | DN93-27 | DN93-28 | F93FRIJ6 | SLR93-1 |
|---|---|---|---|---|---|---|---|---|---|---|---|---|
| SiO2 | 52.65 | 51.22 | 51.57 | 51.63 | 51.69 | 57.99 | 55.06 | 53.8 | 51.63 | 51.69 | 57.99 | 55.06 |
| TiO2 | 1.53 | 1.49 | 1.49 | 1.49 | 1.48 | 0.94 | 1.51 | 1.31 | 1.49 | 1.48 | 0.94 | 1.51 |
| Al2O3 | 17.39 | 15.72 | 16.73 | 16.14 | 16.2 | 16.08 | 18.75 | 15.77 | 16.14 | 16.2 | 16.08 | 18.75 |
| Fe2O3 | 8.87 | 11.54 | 9.27 | 11.32 | 11.33 | 6.83 | 8.65 | 8.56 | 11.32 | 11.33 | 6.83 | 8.65 |
| MnO | 0.14 | 0.16 | 0.15 | 0.16 | 0.16 | 0.11 | 0.09 | 0.14 | 0.16 | 0.16 | 0.11 | 0.09 |
| MgO | 4.66 | 7.35 | 6.47 | 6.71 | 6.55 | 4.51 | 1.82 | 6.11 | 6.71 | 6.55 | 4.51 | 1.82 |
| CaO | 7.54 | 8.82 | 8.54 | 8.96 | 8.99 | 6.88 | 6.03 | 7.73 | 8.96 | 8.99 | 6.88 | 6.03 |
| Na2O | 4.75 | 3.25 | 4.49 | 3.32 | 3.19 | 4.19 | 4.53 | 4.36 | 3.32 | 3.19 | 4.19 | 4.53 |
| K2O | 2.1 | 1.04 | 1.92 | 1.11 | 1.21 | 2.02 | 2.2 | 2.33 | 1.11 | 1.21 | 2.02 | 2.2 |
| P2O5 | 0.64 | 0.31 | 0.94 | 0.31 | 0.31 | 0.43 | 0.64 | 0.85 | 0.31 | 0.31 | 0.43 | 0.64 |
| Total | 100.46 | 100.91 | 101.56 | 101.15 | 101.11 | 99.97 | 99.27 | 100.97 | 101.15 | 101.11 | 99.97 | 99.27 |
| V | 152.27 | 182.12 | 145.95 | 177.43 | 183.34 | 118.01 | 170.36 | 142.82 | 177.43 | 183.34 | 118.01 | 170.36 |
| Cr | 48.58 | 257.55 | 135 | 209.18 | 218.41 | 123.17 | 64.8 | 147.93 | 209.18 | 218.41 | 123.17 | 64.8 |
| Ni | 33 | 119.67 | 96.42 | 99.48 | 102.23 | 90.52 | 35.28 | 124.55 | 99.48 | 102.23 | 90.52 | 35.28 |
| Zn | 91.75 | 99.38 | 82.35 | 88.05 | 87.65 | 85.8 | 83.39 | 79.13 | 88.05 | 87.65 | 85.8 | 83.39 |
| Rb | 28.53 | 17.83 | 28.62 | 18.2 | 19.29 | 29.17 | 36.58 | 38.31 | 18.2 | 19.29 | 29.17 | 36.58 |
| SR | 1367.34 | 446.48 | 1376.64 | 437.34 | 440.47 | 871.81 | 1141.6 | 1115.35 | 437.34 | 440.47 | 871.81 | 1141.6 |
| Y | 25.28 | 29.37 | 25.83 | 28.66 | 26.06 | 21.5 | 24.73 | 27.01 | 28.66 | 26.06 | 21.5 | 24.73 |
| Zr | 275.76 | 145.77 | 270.36 | 148.21 | 149.24 | 214.69 | 277.32 | 241.04 | 148.21 | 149.24 | 214.69 | 277.32 |
| Nb | 43.78 | 17.83 | 46.29 | 20.14 | 19.3 | 27.62 | 35.59 | 40.98 | 20.14 | 19.3 | 27.62 | 35.59 |
| Ba | 1199.3 | 383.62 | 1177.81 | 389.44 | 460.28 | 1090.93 | 1178.7 | 1588.92 | 389.44 | 460.28 | 1090.9 | 1178.7 |

**Pajarito Canyon**
holeiite DN86-1b
DN93-13 dike 3.18+-0.38 Ma
lugearite/hawaiite DN86-1a 2.46+-0.02 Ma

**Water Canyon**
Tholeiite DN85-141 2.39+-0.08 Ma
Mugearite DN85-104
DN85-14 2.50+-0.04 Ma
Mugearite DN86-4

**West of Water Canyon**
Mugearite DN93-8 2.59+-0.18 Ma

**Between Ancho and Chaquehui Canyons**
Hawaiite DN93-25 2.39+-0.08 Ma
Mugearite dike DN93-26 2.54+-0.02 Ma

**Ancho Canyon**
Tholeiite DN85-140
DN93-27 2.48+-0.06 Ma
DN93-28 2.36+-0.06 Ma
Benmorite DN85-139b
Mugearite DN85-137
SLR93-1 9.3+-0.20 Ma

**Chaquehui Canyon**
Tholeiite DN93-5 2.45+-0.06 Ma
AWL-1-93
Tholeiite DN85-129 2.78+-0.04 Ma

**Frijoles Canyon**
Benmorite F93-FRIJ-6 2.75+-0.08 Ma

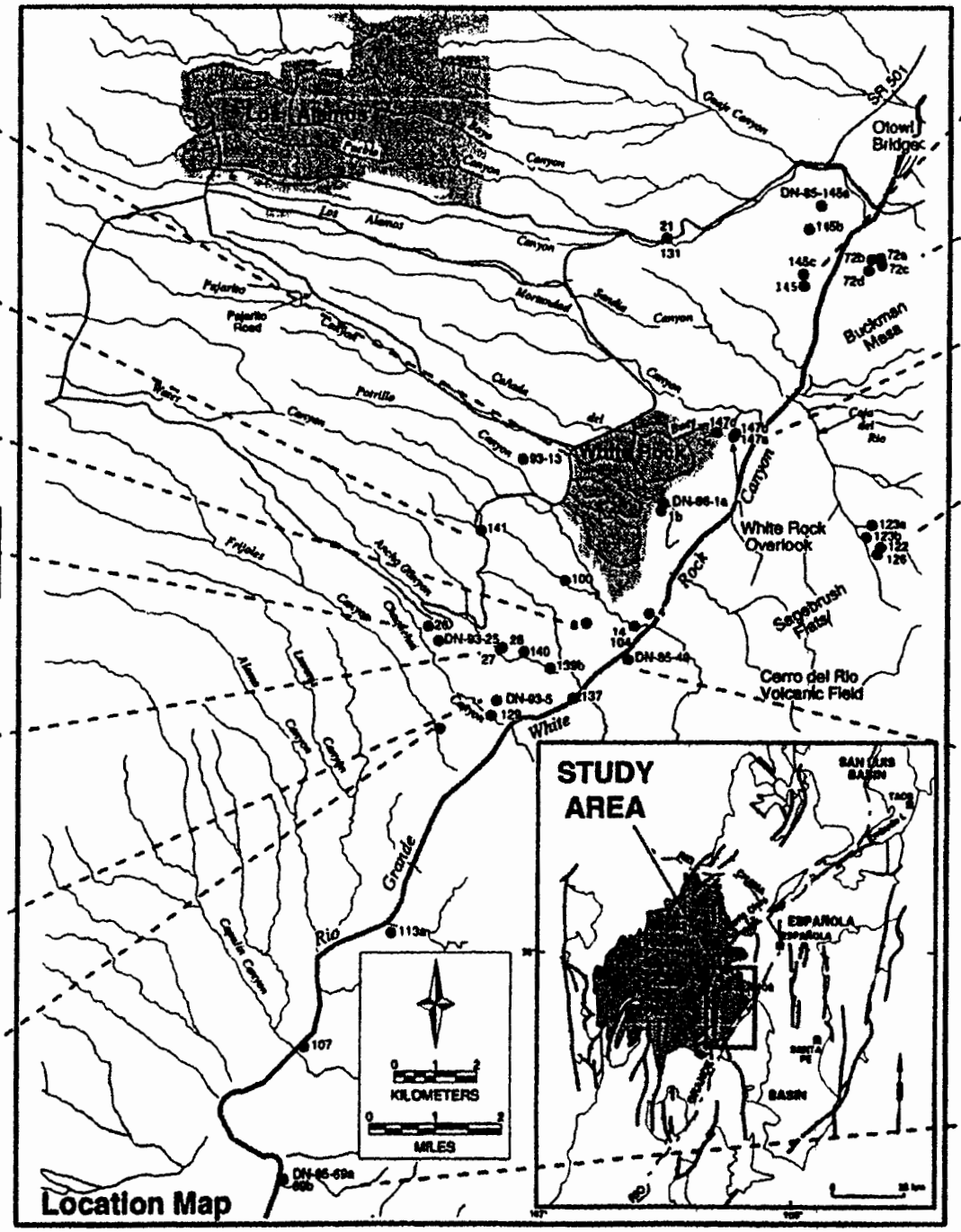


**Los Alamos Canyon**
Tholeiite DN85-131
DN93-21 2.33+-0.08 Ma
Mugearite DN85-145a 2.57+-0.02 Ma
DN85-145c 2.55+-0.02 Ma

**La Mesita Cinder Cone**
Mugearite/Hawaiite DN85-72a,c
Mugearite DN85-72b,d

**White Rock Overlook**
Tholeiite DN85-147c 2.46+-0.03 Ma
Mugearite DN85-147b 2.50+-0.02 Ma

**Caja del Rio Canyon**
Hawaiite DN85-122 2.49+-0.03 Ma
DN85-123b
Tholeiite DN85-126

**East of Rio Grande from Water canyon**
Hawaiite DN85-40 2.54+-0.06 Ma

**North of Cochiti Dam**
Mugearite DN85-69a,b
Dacite DN85-107
DN85-113a

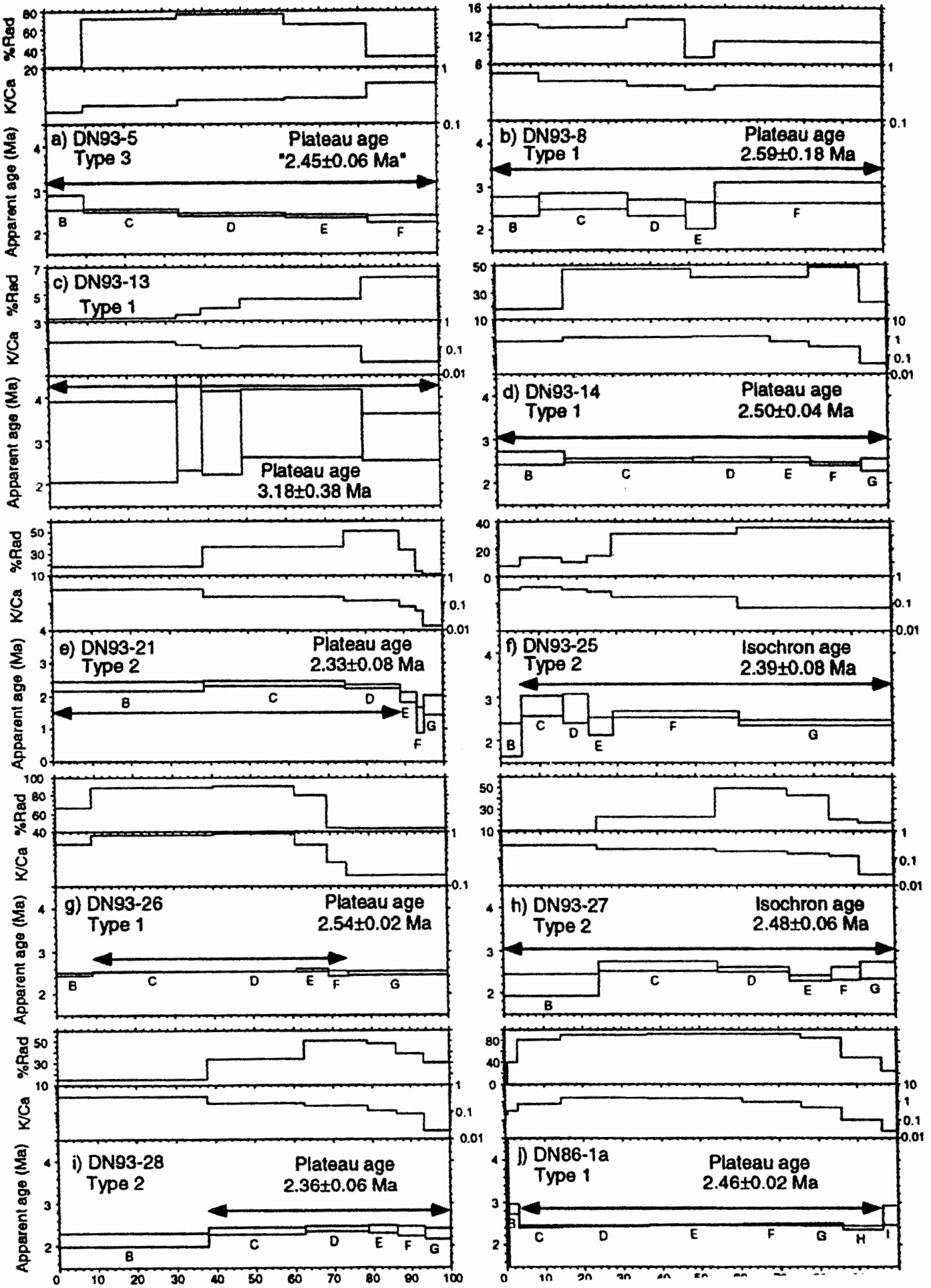
a) DN93-5
Type 3
Plateau age
"2.45±0.06 Ma"
b) DN93-8
Type 1
Plateau age
2.59±0.18 Ma
c) DN93-13
Type 1
Plateau age
3.18±0.38 Ma
d) DN93-14
Type 1
Plateau age
2.50±0.04 Ma
e) DN93-21
Type 2
Plateau age
2.33±0.08 Ma
f) DN93-25
Type 2
Isochron age
2.39±0.08 Ma
g) DN93-26
Type 1
Plateau age
2.54±0.02 Ma
h) DN93-27
Type 2
Isochron age
2.48±0.06 Ma
i) DN93-28
Type 2
Plateau age
2.36±0.06 Ma
j) DN86-1a
Type 1
Plateau age
2.46±0.02 Ma
%Rad
K/Ca
Apparent age (Ma)

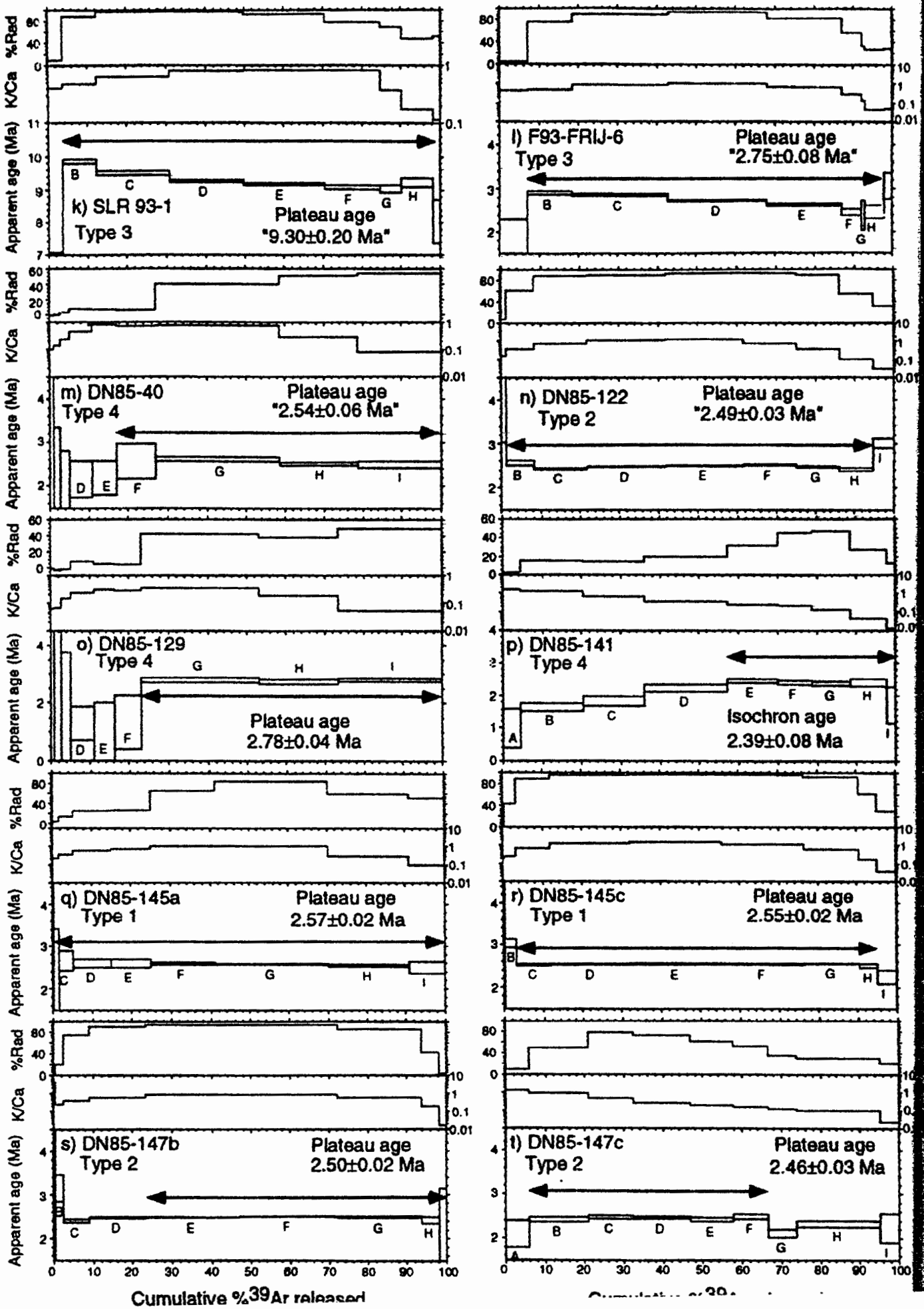
k) SLR 93-1
Type 3
Plateau age
"9.30±0.20 Ma"
l) F93-FRIJ-6
Type 3
Plateau age
"2.75±0.08 Ma"
m) DN85-40
Type 4
Plateau age
"2.54±0.06 Ma"
n) DN85-122
Type 2
Plateau age
"2.49±0.03 Ma"
o) DN85-129
Type 4
Plateau age
2.78±0.04 Ma
p) DN85-141
Type 4
Isochron age
2.39±0.08 Ma
q) DN85-145a
Type 1
Plateau age
2.57±0.02 Ma
r) DN85-145c
Type 1
Plateau age
2.55±0.02 Ma
s) DN85-147b
Type 2
Plateau age
2.50±0.02 Ma
t) DN85-147c
Type 2
Plateau age
2.46±0.03 Ma
%Rad
K/Ca
Apparent age (Ma)
Cumulative %39Ar released

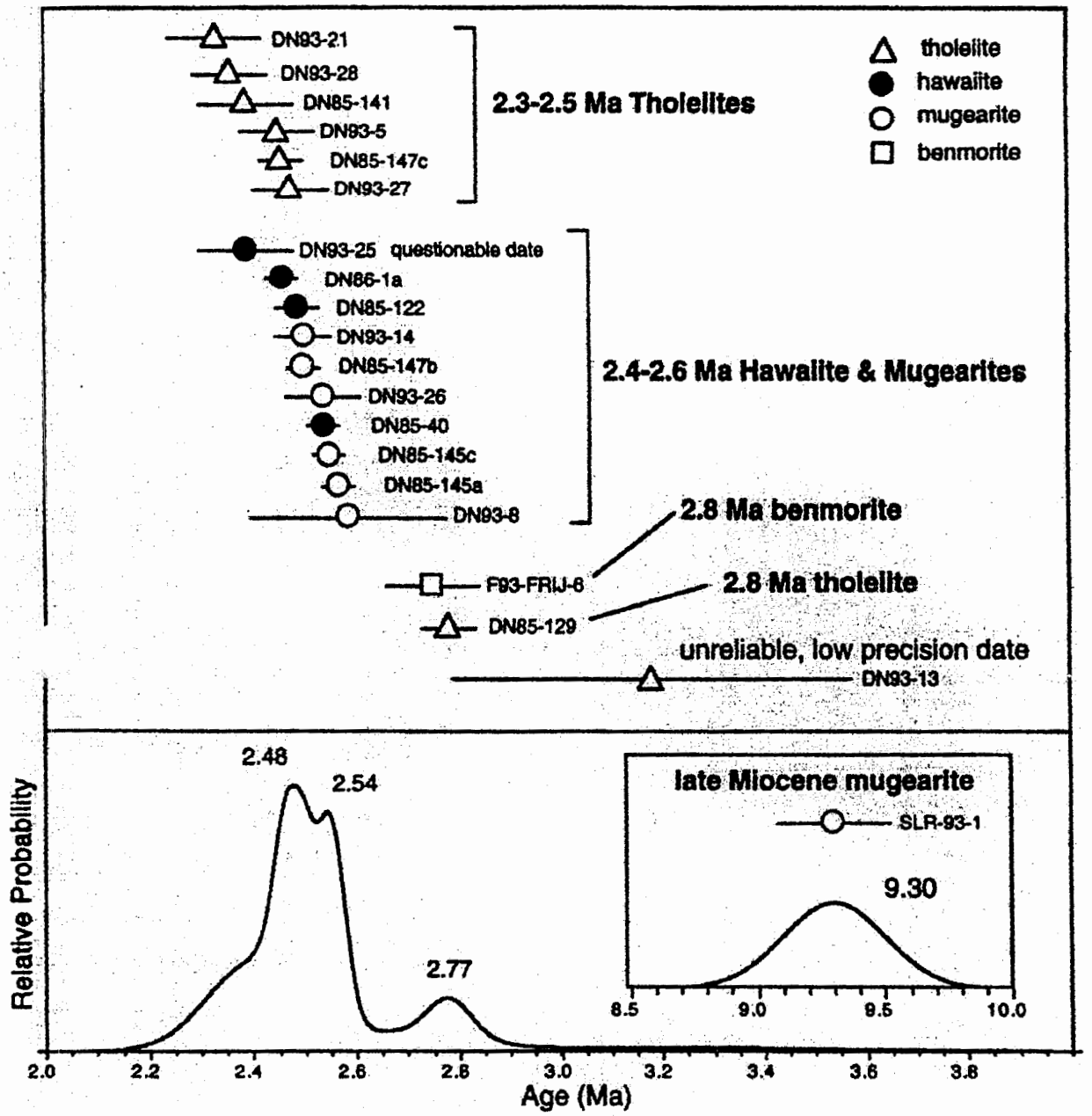
DN93-21
DN93-28
DN85-141
DN93-5
DN85-147c
DN93-27
2.3-2.5 Ma Tholeiites
tholeiite
hawaiite
mugearite
benmorite
DN93-25 questionable date
DN86-1a
DN85-122
DN93-14
DN85-147b
DN93-26
DN85-40
DN85-145c
DN85-145a
DN93-8
2.4-2.6 Ma Hawaiite & Mugearites
2.8 Ma benmorite
F93-FRIJ-6
2.8 Ma tholeiite
DN85-129
unreliable, low precision date
DN93-13
Relative Probability
2.48
2.54
2.77
2.0
2.2
2.4
2.6
2.8
3.0
3.2
3.4
3.6
3.8
Age (Ma)
late Miocene mugearite
SLR-93-1
9.30
8.5
9.0
9.5
10.0

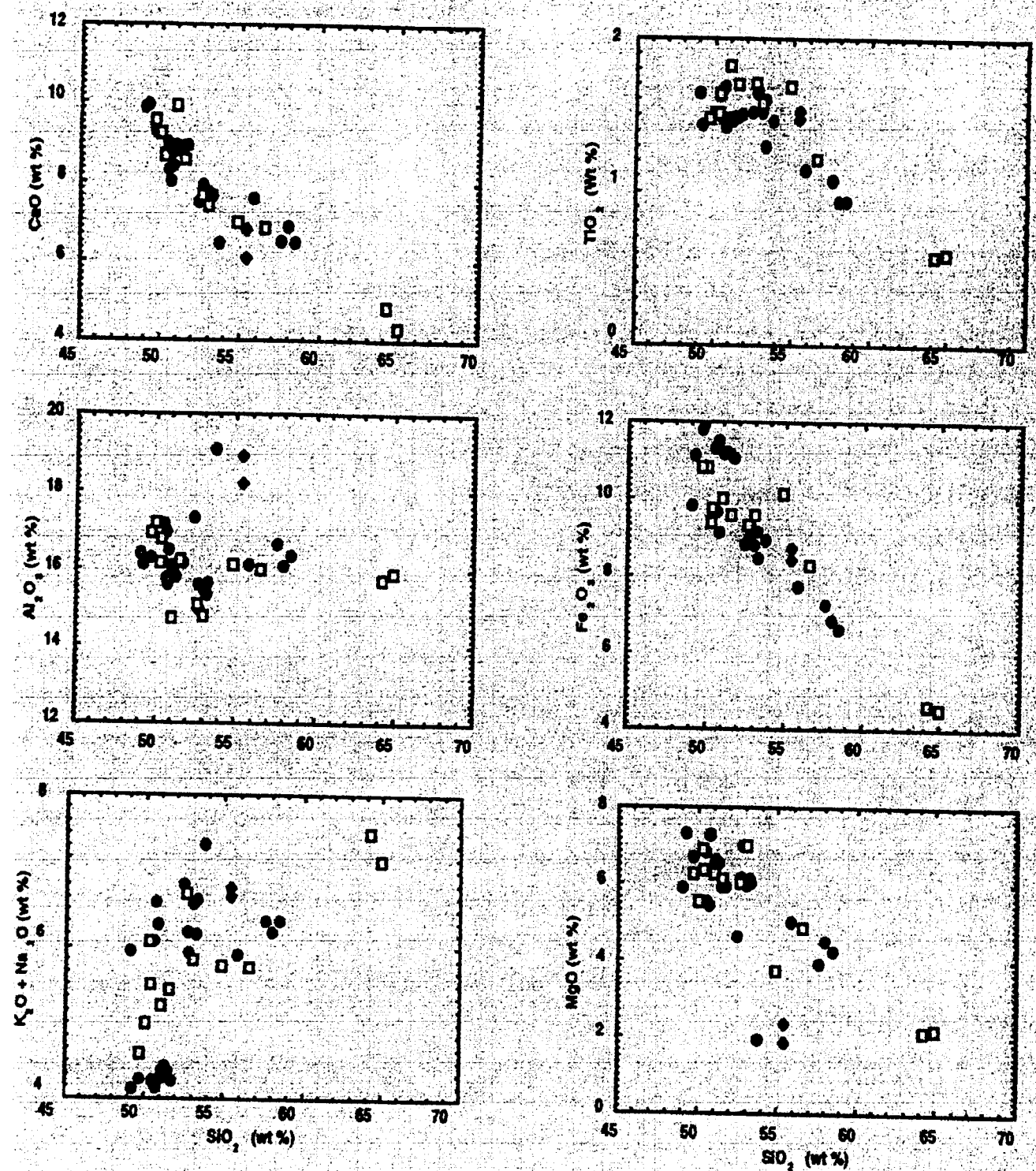
CaO (wt %)
TiO2 (Wt %)
Al2O3 (wt %)
Fe2O3 (wt %)
K2O + Na2O (wt %)
MgO (wt %)
SiO2 (wt %)
SiO2 (wt %)

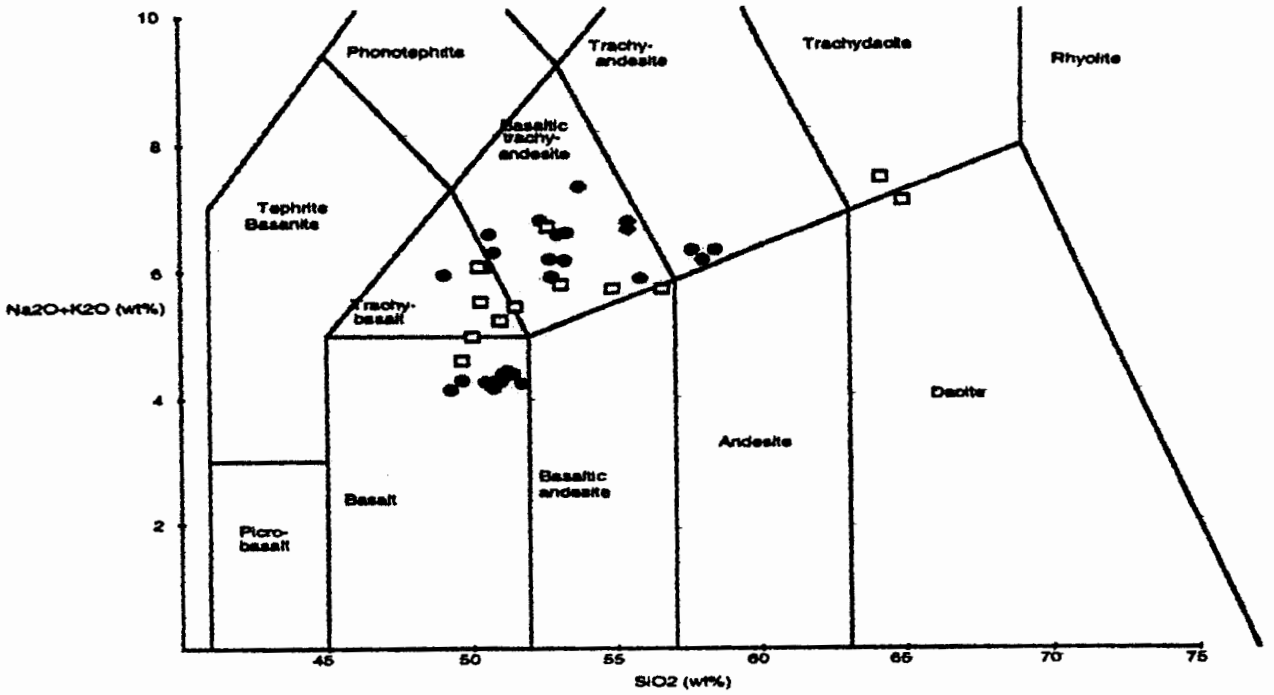


Figure 5

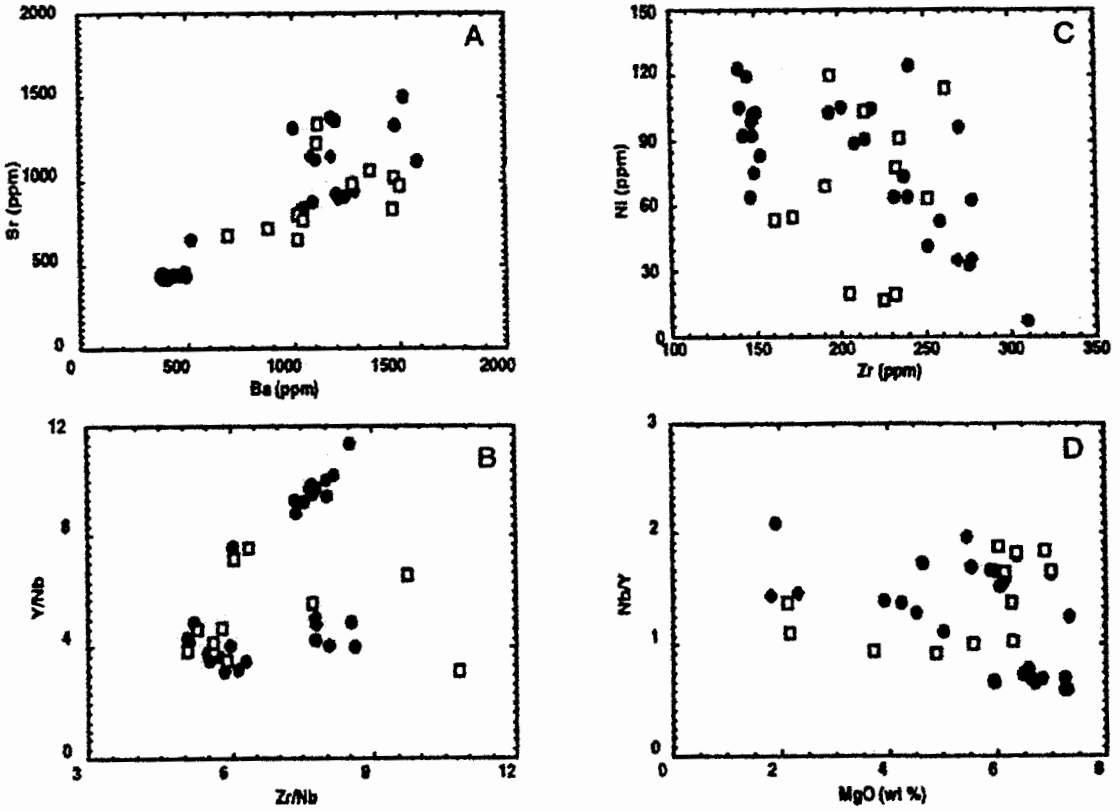


Figure 6